Resistance of Si_3N_4 ceramic tools to thermal and mechanical loading in cutting of iron alloys

R. F. Silva[a], J. M. Gomes[b], A. S. Miranda[b] and J. M. Vieira[a]

[a]*Departamento de Engenharia Cerâmica e do Vidro, Universidade de Aveiro, 3800 Aveiro (Portugal)*

[b]*Departamento de Engenharia Mecânica, Universidade do Minho, 4800 Guimaraes (Portugal)*

(Received August 29, 1990; revised January 8, 1991; accepted January 30, 1991)

Abstract

The mechanisms of wear in two extreme cases relating to the performance of Si_3N_4-based cutting tools in machining iron alloys were investigated, with the corresponding wear rates correlated with cutting speed, tool and alloy composition and seizure. The sources of discrepancy between the cutting tests and conventional pin-on-disk tests are discussed on the basis of loads, surface speed, wear debris accumulation, reaction with atmospheric oxygen and solid lubrication.

The distinct interactions with the ceramic tool of a hard, high temperature deformable alloy and a brittle, composite-like alloy with, in addition, self lubrication at high temperature, yield great differences in the amount of heat generated during the process. The selective corrosion of the ceramic grain boundary phase and the abrasion through grain pullout and ploughing are changed according to the effects of temperature on the metal–ceramic contact surface.

1. Introduction

Current efforts in cutting technology are concerned with the high speed machining of highly resistant alloys. Developments in equipment and tool materials have led to significant improvements in this area [1, 2]. A class of new materials — ceramics — seems to be capable of coping with such demands, either as bulk, composite or coatings. Ceramics can attain removal rates of 12×10^{-6} m^3 s^{-1}, the tool lives being adequate to reduce costs in the fast production of automotive components. Ceramics also provide the only way to work economically the hard machinable alloys in the aerospace industry.

In high speed cutting, the metal undergoes strain conditions comparable only with those found in ballistics or in the explosive working of metals. Strain rates of 10^5 s^{-1} [3], characteristic times (time required to produce 1% strain) of 10^{-7} s [3] and compressive stresses as high as 1.8 GPa [4] have been reported. Shear strains in the condition of seizure can reach values of 600 [4]. The temperature at the contact between chip and tool can rise up to 1200 °C [5].

The refractoriness of ceramics usually provides good mechanical response at high temperature, but their thermal shock resistance at moderately high temperatures is often poor if compared with the more conventional cutting materials, such as hard metals. In high speed cutting, failure can also result from chemical loading. This is a serious limitation to the performance of ceramics, such as Si_3N_4 materials, which are known to exhibit good behavior in high temperature and thermal fatigue loading,

0043-1648/91/$3.50

but suffer from early failure in applications of great economical potential such as steel cutting.

The mechanisms of wear in two extreme cases relating to the performance of Si_3N_4-based cutting tools are investigated in the present study. The most favorable case is gray cast iron machining, and the destructive test is tool steel machining. As the tool–workpiece interactions in cutting are very complex and thus difficult to reproduce in laboratory tests, cutting tests are still the best approach to tool wear evaluation. Wear tests, such as the conventional or modified [6, 7] pin-on-disk tests, when used with a good knowledge of material properties, can be helpful. Two Si_3N_4 ceramics – β-Si_3N_4 and SiAlON with CeO_2 additions – are compared. Superior chemical resistance and high fracture toughness of Si_3N_4 materials doped with this rare earth oxide have been reported [8–10].

2. Materials and experimental procedures

Tool materials were prepared from Si_3N_4 (HCStarck LC10 for β-Si_3N_4 and LC12 for CeSiAlON), AlN (HCStarck Grade C) and CeO_2 (Fluka) powders by uniaxial hot pressing. The molar compositions of the ceramic inserts are given in Table 1. The relative densities are all above 0.99. The crystalline phase composition, particle size and mechanical properties of the ceramic materials are given in Table 2.

Gray cast iron and high-carbon high-chromium tool steel were selected for the wear and cutting tests; the properties are given in Table 3. Phase composition was determined from the peak intensity ratio of the X-ray diffraction measurements as

TABLE 1

Molar compositions of tool materials

Tool material	Si_3N_4 (mol.%)	SiO_2 (mol.%)	Ce_2O_3 (mol.%)	AlN (mol.%)
β-Si_3N_4	87.4[a]	10.6	2.0	–
CeSiAlON	74.0[b]	7.3	1.7	17.0

Maximum impurity content by weight: [a]LC10, Fe, 0.04%; Al, 0.10%; Ca, 0.03%; [b]LC12, Fe, 0.008%; Al, 0.045%; Ca, 0.008%.

TABLE 2

Crystalline phase composition, microstructural parameters and mechanical properties of the tool materials

Tool material	β (%)	α (%)	HV1 (GPa)	K_{IC} (MPa $m^{1/2}$)	σ_f (MPa)	l (μm)	d (μm)	AR[a]
β-Si_3N_4	100	0	14.7 (σ=0.6)	4.2 (σ=0.3)	530	5.2	1.2	4.3
CeSiAlON	67.5	32.5	18.3 (σ=0.5)	4.3 (σ=0.1)	726	1.3	0.3	4.6

[a]AR (aspect ratio)=l (grain length)/d (grain width).

TABLE 3

Properties of the workpiece materials

Material	Code	Composition	Hardness
Gray cast iron	Grade 200	3.9% C; 2.9% Si; 0.9% Mn 0.04% (max) S; 0.1% (max)	195 BHN
Annealed TS2080	DIN 1.2080	2.0% C; 12% Cr	250 HV15
Hardened TS2080	DIN 1.2080	2.0% C; 12% Cr	710 HV15

$$\alpha\,(\%) = \frac{\{\alpha\text{-}I(210) + \alpha\text{-}I(201)\}}{\{\alpha\text{-}I(210) + \alpha\text{-}I(201) + \beta\text{-}I(101) + \beta\text{-}I(210)\}} \times 100 \quad (1)$$

$$\beta\,(\%) = 100 - \alpha\,(\%) \quad (2)$$

The room temperature hardnesses of the alloys and ceramics were determined as follows. The hardness of the iron alloys was measured using a Vickers indenter with a load of 147 N. The hardness of the Si_3N_4 ceramics was measured using a Vickers indenter with a load of 9.8 N and a loading speed of 0.017 mm s^{-1}; the hardness is the average of 20 indentations for each sample.

The indentation fracture toughness K_{IC} was determined according to Niihara's expression [11]. The three-point bending strength σ_f was determined with chamfered bars (4 mm×5 mm×25 mm) at a loading speed of 0.167 mm s^{-1}. The present values of σ_f are the average of three results for each material.

A conventional tri-pin-on-disk machine was used for non-lubricated wear tests against gray cast iron and hardened tool steel in air at room temperature. Conical flat-end pins with 1 mm of initial contact diameter were weight loaded over the metal disk. The frictional force was measured using a bending beam and strain gauge elements. Load and sliding speed were kept constant at values of 3.9 N and 0.5 m s^{-1} respectively. The tri-pin-on-disk tests were stopped at regular time intervals for measurement of the weight losses of the worn pins within the 10^{-5} g accuracy limit. Volume wear was calculated from the weight loss and the specific weight of the ceramic. After running-in, the tribological pair entered steady state conditions and the wear volume V was observed to be proportional to the sliding distance d with a constant slope. The friction coefficient μ was calculated from the normal load and the sliding frictional force. The wear coefficient K corresponding to the steady state conditions is defined as

$$K = V/(Pd) \quad (3)$$

where V is the volume loss after running-in, d is the sliding distance after running-in and p is the normal load.

Hot pressed samples were machined to the normalized indexable insert geometry ISO SNGN 120808 20°-T chamfered. The insert holder was of CSRN 2525 M12 type (ISO 1832). Cutting tests with gray cast iron and annealed tool steel were carried out without coolant in a numerically controlled lathe. Average cutting speeds were calculated by accounting for the workpiece radius reduction at constant angular speed. The removal rate Q is the product of the cutting speed, the feed and the depth of cut (DOC). The volume of removed material M was calculated as Qt, where t is the total time. The following conventional tool wear parameters were measured: VB, mean

flank wear; KT, maximum crater depth; KM, distance between tool edge and crater center.

The tool wear parameters were measured using optical microscopy. Due to metal covering of the clearance face in gray cast iron machining, VB is overestimated by this technique of observation. The crater wear rate was calculated as $\Gamma_K = (KM \times KT)/t$. The metal removal rate was normalized by the depth of cut (DOC): $M_c = M_r/(DOC) \times t$. The crater wear resistance was calculated as the ratio $\epsilon = 1/(\Gamma_K/M_c)$.

The grain size and grain aspect ratio were determined from chord length measurements (obtained from scanning electron micrographs of polished and chemically etched surfaces) according to the relationships established for hexagonal prisms [12] and for the a_{95} ratio parameter [13]. The worn surfaces and the wear debris were investigated by scanning electron microscopy (SEM) with energy dispersive spectroscopy (EDS).

3. Results

The Si_3N_4 ceramics were pressure sintered through a liquid phase mechanism. Si_3N_4 oxidation resulting from CeO_2 reduction to Ce_2O_3 at $T > 1500$ °C increases the amount of sintering-aiding liquid in the CeO_2-doped Si_3N_4 samples. The total SiO_2 content (after oxidation of Si_3N_4) is given in Table 1. AlN dissolves in the glass decreasing the viscosity of the liquid and improving the densification rate. The CeSiAlON composition will hypothetically attain the $M/X = 3/4$ plane in Janecke's representation of the quasiquaternary system Si_3N_4–AlN–CeN–Ce_2O_3–Al_2O_3–SiO_2 towards β'-SiAlON solid solution development [14]. High refractoriness of the intergranular phases of the SiAlON will then be achieved. The nitrogen in the final intergranular phases improves the creep resistance of the material [15, 16]. By sintering some of the compositions at low temperatures, the fine grain, equiaxial α phase is partially retained.

3.1. "Pin-on-disk" tests

The tribological coefficients of each ceramic–metal pair are presented in Table 4.

Broadly polished worn ceramic surfaces of the β-Si_3N_4–steel contact were observed (Fig. 1(a)). The surfaces became rougher towards the side edges (Fig. 2(a)). The wear debris adherent to the worn surface was concentrated on the pin escape zone (Fig. 2(b)). Semiquantitative SEM–EDS elemental analysis of iron and cerium (Fig. 3(a)) over the zones corresponding to the intergranular phase, the top of the Si_3N_4 grains and the composite wear debris adhesions showed that there was a correlation between

TABLE 4

Tribological coefficients of the metal–ceramic pairs

Pin–disk	Friction coefficient	Pin wear coefficient K (MPa^{-1})
β-Si_3N_4–hardened TS2080	0.76	1.8×10^{-14}
β-Si_3N_4–gray iron	0.85	1.0×10^{-14}
CeSiAlON–gray iron	0.62	1.7×10^{-14}
CeSiAlON–hardened TS2080	0.77	8.7×10^{-15}

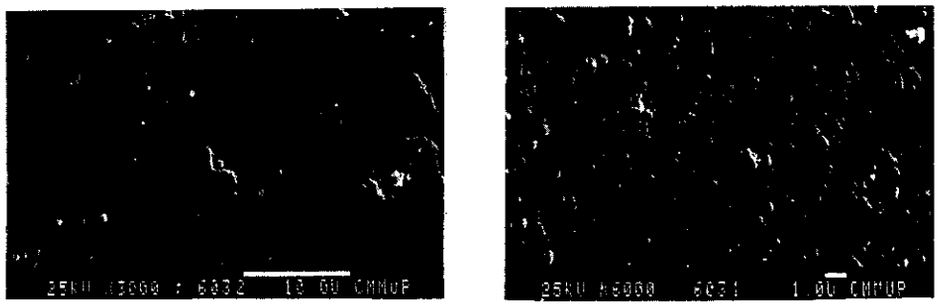

(a) (b)

Fig. 1. (a) Ceramic pin surface of the β-Si_3N_4–tool steel contact (SEM/BS). (b) Ceramic pin surface of the β-Si_3N_4–gray cast iron contact (SEM/BS). (BS — back scattered electron image.)

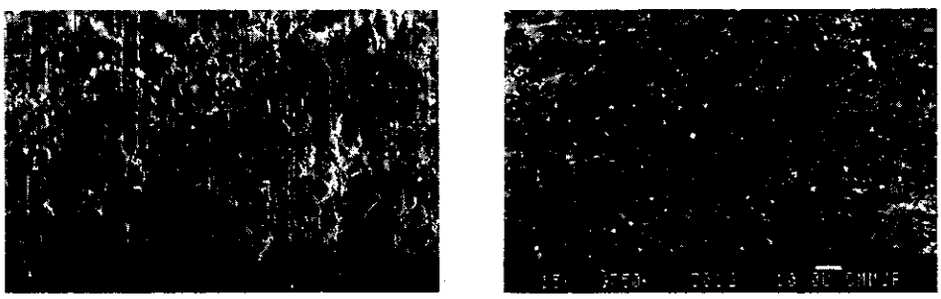

(a) (b)

Fig. 2. Local features of the worn pin surface: (a) pin surface as the side edge is approached (SEM/ES); (b) pin escape zone (SEM/ES). (ES — secondary electron image.)

iron surface enrichment, worn surface and the composition of the ceramic grain boundary phase (Fig. 3(b)). The worn ceramic surfaces of the β-Si_3N_4–gray cast iron pairs were also polished (Fig. 1(b)); fine grooving and grain boundary weakening were observed.

The corresponding wear tracks on the metallic disks were covered by a thick reaction layer, mainly glassy silicate reaction products and iron oxides. The wear debris was composed of Si–Fe oxidized particles and plates and metallic particles (Fig. 4), the former being larger and more abundant than the metallic particles. Fracture of the tribological layer of the disk wear track showed that thermal and/or mechanical fatigue of the glassy layer occurred under the cyclic loading of the pins.

3.2. Cutting tests

Typical wear patterns of β-Si_3N_4 tool inserts against tool steel and gray cast iron are shown in Fig. 5. The general features of the heavy cratering on the rake face can be seen in Fig. 5(a): adherent metal scraps in the crater leading region and an extensively abraded region from the middle to the trailing edge of the crater. A continuous, narrow layer covering the escape chip–tool contact was also observed (Fig. 5(a)).

The crater morphologies of the β-Si_3N_4 and CeSiAlON inserts after cutting of tool steel and gray cast iron are compared in Fig. 6. As observed for the inserts in

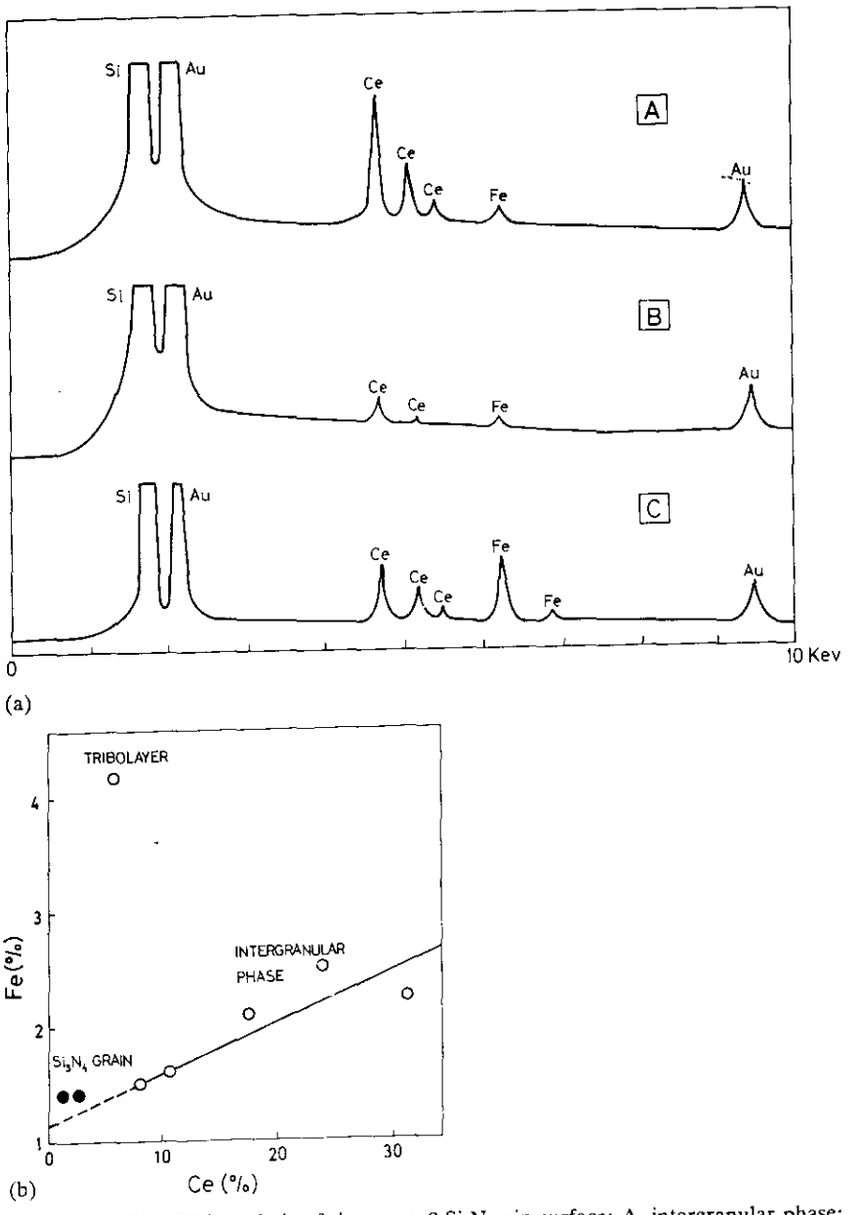

Fig. 3. (a) SEM–EDS analysis of the worn β-Si_3N_4 pin surface: A, intergranular phase; B, Si_3N_4 grain; C, wear debris adhesion. (b) Correlation between iron and cerium concentration over the worn pin surface of the β-Si_3N_4–TS2080 pair.

Fig. 5, both Si_3N_4 materials showed rapid cratering after tool steel cutting (Fig. 6(a) and 6(b)) and high wear resistance after cutting of gray cast iron (Fig. 6(c) and 6(d)). The CeSiAlON insert exhibited better edge preservation in steel cutting (Fig. 6(b))

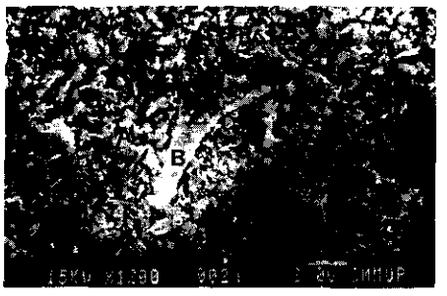

Fig. 4. Wear debris from β-Si_3N_4–tool steel contacts: A and B, Si–Fe oxidized particle and plate; C, metallic particle (SEM–EDS chemical analysis).

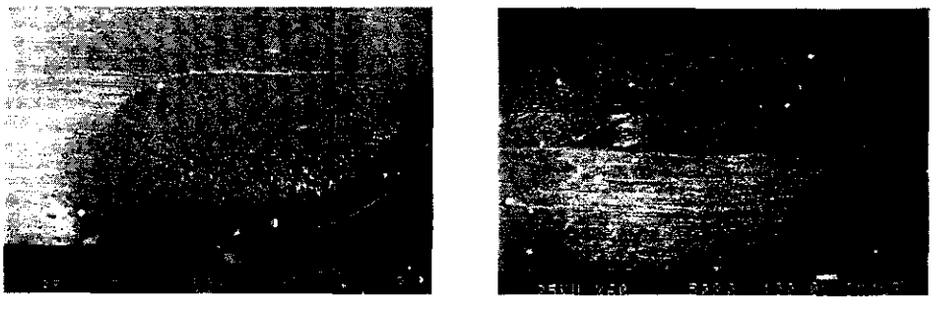

(a) (b)

Fig. 5. (a) Top view of the crater land of a β-Si_3N_4 insert after tool steel machining (3.6 m s^{-1}; DOC = 1 mm) (SEM/BS). (b) General view of the wear pattern after β-Si_3N_4–gray cast iron turning (3.6 m s^{-1}; DOC = 1 mm) (SEM/BS).

The top views of the rake face and the topography of the wear land of the ceramic inserts after cutting of the iron alloys are presented in Fig. 7. The chemical compositions of the prominent features of the worn surfaces are given in Fig. 8.

The top view of the crater in Fig. 7(a) appeared to be identical to the crater in Fig. 5(a) except for the large, oxidized iron deposit which was formed under the intermittent contact between the chip and the insert following the continuous contact in the crater. Cracking of the deposit was observed at higher magnification (Fig. 9(a)). Silicon and iron were detected by EDS analysis of the crazed deposit (Fig. 8); this glass-like layer is the product of the reaction between the chip, the ceramic tool and atmospheric oxygen.

Iron scraps in the crater leading region are clearly seen in Fig. 7(b). EDS chemical analysis revealed the presence of iron and chromium (Fig. 8). The topography of the worn ceramic surfaces varied from this point to the crater and the clearance face (Fig. 9(a), 9(b) and 9(c)). The extremely plastically deformed region corresponding to the trailing region of the crater was almost free of adherent metal (Fig. 9(b)), but a narrow terminal deposit accumulated in the escape zone. This deposit (also observed in Fig. 5(a)) was very rich in ceramic intergranular elements, mainly cerium and the impurities calcium and aluminum (Fig. 8), dissolved iron from the chip was also detected. Unlike the contacts between β-Si_3N_4 and tool steel, the iron and chromium deposit observed after cutting of tool steel by CeSiAlON (Fig. 7(c)) extended all over

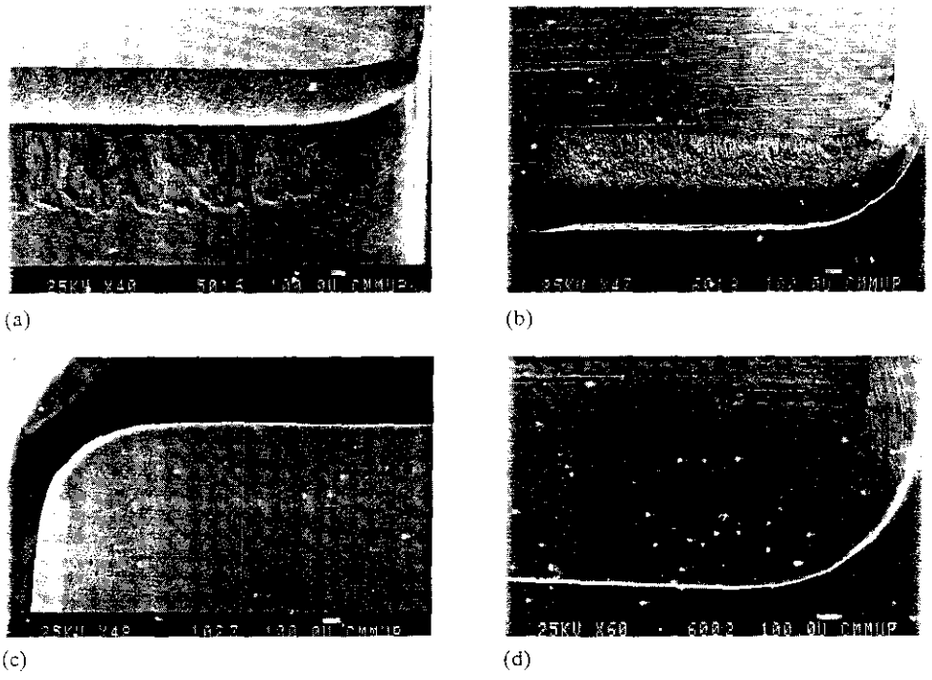

Fig. 6. (a) Crater and flank wear of a β-Si_3N_4 insert after high speed machining of tool steel (3.6 m s^{-1}; DOC=4 mm) (SEM/ES). (b) Top view of the CeSiAlON crater land after high speed machining of tool steel (3.9 m s^{-1}; DOC=4 mm) (SEM/ES). (c) Top view of the rake face of a β-Si_3N_4 insert after a long period gray cast iron turning test ($M_t = 944 \times 10^{-6}$ m^3) (SEM/ES). (d) Top view of the CeSiAlON insert tested against gray cast iron ($M_t = 1165 \times 10^{-6}$ m^3) (SEM/ES).

the crater land, whereas the effects of mecnanical abrasion were less evident (Fig. 7(d)).

Thick adherent iron layers due to flank wear were observed on the clearance face for the higher removal rate tests (DOC=4 mm) (Figs. 9(c), 10(a) and 10(b)).

The cutting edges of the Si_3N_4 inserts were almost preserved in gray cast iron machining (Figs. 5(b), 6(c) and 6(d)). The insert in Fig. 5(b) was tested under similar cutting conditions as that presented in Fig. 5(a). The top view of the rake contact for longer times of testing is shown in Fig. 6(c); little crater wear was observed. Two different barrier deposits were observed beyond the crater — the first was mainly composed of MnS (Fig. 8) and the second was rich in iron, similar to that observed in the corresponding intermittent contact regions in the ceramic–steel tests (Fig. 7(a)). The iron contamination, coming from the workpiece, was generally low at the rake contact surface (Figs. 7(e), 7(f) and 8). The machining tests with the CeSiAlON inserts were carried out at higher cutting speeds. Even then these inserts were only slightly damaged as can be seen in Fig. 6(d) for the rake contact and in Fig. 10(c) for the clearance face. Fine grooving was observed on the rake contact surface (Fig. 7(f)). The narrow flank wear region at the leading edge of the clearance face was followed by a large metallic deposit which protected the ceramic surface from wear (Fig. 10(c)).

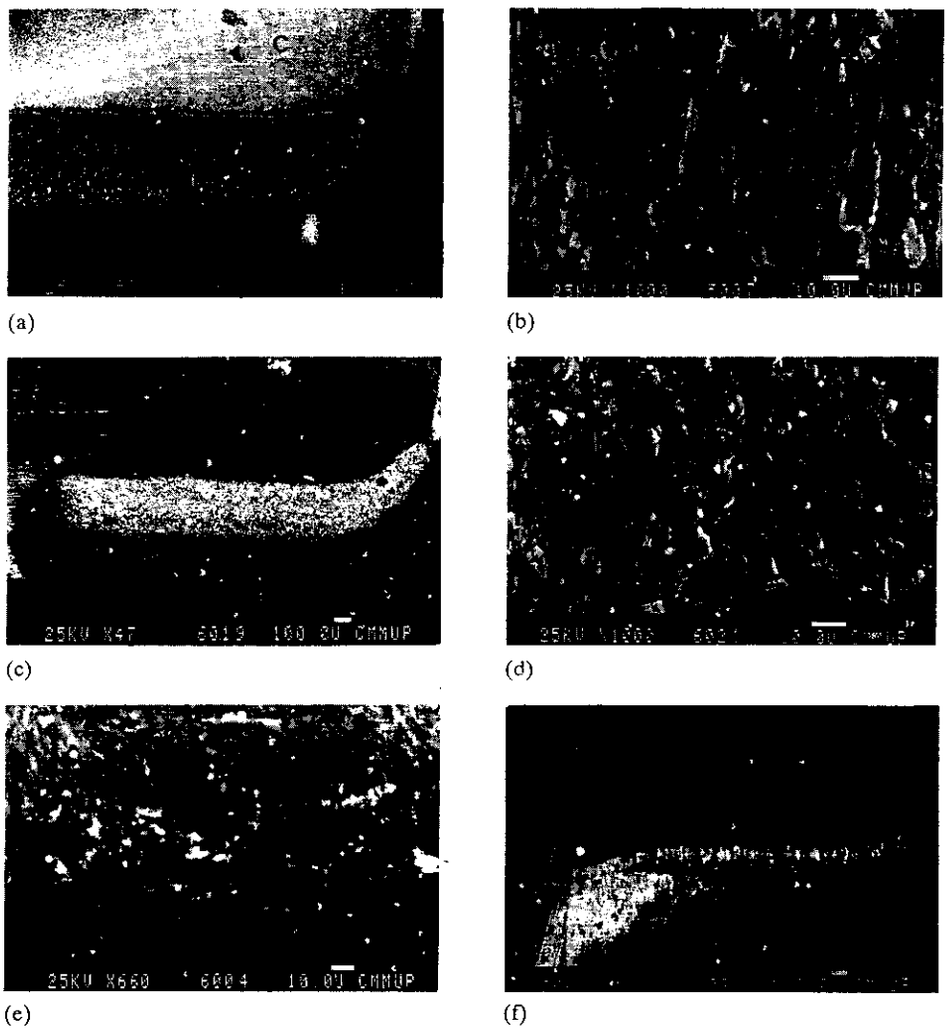

Fig. 7. (a) Chemically contrasted pattern of the crater after a β-Si_3N_4–tool steel test (3.6 m s^{-1}; $t = 15$ s) (SEM/BS). (b) High magnification of the crater leading zone after β-Si_3N_4–tool steel machining (3.6 m s^{-1}; $t = 15$ s) (SEM/BS). (c) Wear pattern of the rake face after CeSiAlON–tool steel turning (3.9 m s^{-1}; $t = 12$ s) (SEM/BS). (d) High magnification of the worn crater land after CeSiAlON–tool steel machining (3.9 m s^{-1}; $t = 12$ s) (SEM/BS). (e) Top view of β-Si_3N_4 rake face after long period gray cast iron machining (3.1 m s^{-1}; $t = 610$ s) (SEM/BS). (f) High magnification of the typical pattern of the rake face worn land after gray cast iron machining with β-Si_3N_4 tools (CeSiAlON; 8.5 m s^{-1}; $t = 275$ s) (SEM/BS).

The chips from the cast iron machining with the Si_3N_4 tool were of a discontinuous type in the form of small fragments (Fig. 11(b)). The chips were fractured due to the brittle behavior of graphite flakes in shear. The torn appearance of the steel chip is shown in Fig. 11(a). The extent of plasticity of the steel chip was revealed by carbide contrasting of a polished longitudinal section of the chip (Fig. 12). The surface of

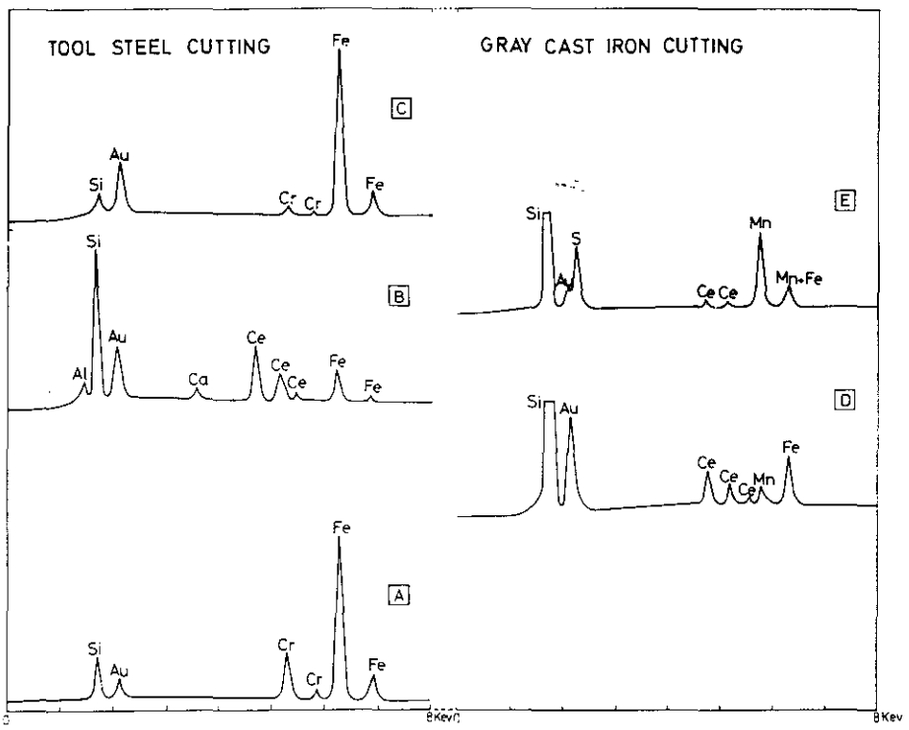

Fig. 8. SEM-EDS chemical analysis of the prominent features of the β-Si_3N_4 crater lands after cutting of the iron alloys. Tool steel (Fig. 7(a)): A, crater leading edge; B, narrow layer at the escape chip–tool contact; C, oxidized iron deposit. Gray cast iron (Fig. 7(e)): D, crater wear land; E, escape chip–tool contact.

the chip (underside view) (Fig. 11(c)) replicated the relief of the highly abraded counter surface at the crater trailing edge (Fig. 9(b)).

The cutting parameters and wear measurements for the ceramic–cast iron and ceramic–steel cutting tests are presented in Table 5. The crater wear rates of both types of Si_3N_4 ceramic inserts in tool steel cutting increased with the metal removal rate (Fig. 13). A simple proportionality was observed for the CeSiAlON inserts (Fig. 13(a)), with a crater wear resistance at low cutting speed three times higher than for the β-Si_3N_4 inserts (Fig. 13(b)). Although the β-Si_3N_4 insert showed an increased crater wear rate at moderate cutting speeds (approximately 3.7 m s^{-1}), CeSiAlON retained the wear rate values obtained for low speed cutting conditions. In addition, for this composition, the flank wear was lower than for the β-Si_3N_4 inserts (Table 5).

The crater wear of the β-Si_3N_4 and CeSiAlON inserts after the cutting of gray cast iron was difficult to measure for the short times given in Table 5. The crater wear resistance ϵ was two orders of magnitude higher than in the tool steel cutting tests. The same trend was observed for the flank wear resistance, but both types of Si_3N_4 inserts showed similar values of flank wear (Table 5).

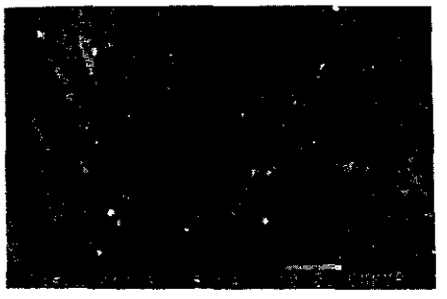

(a)

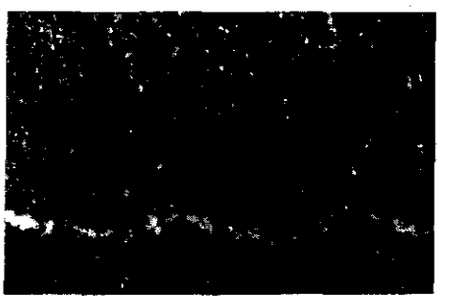

(b)

(c)

Fig. 9. (a) Extensive iron-rich deposit formed during intermittent chip–tool contact (β-Si_3N_4–tool steel machining) (SEM/ES). (b) Trailing edge of the β-Si_3N_4 crater land in tool steel machining (SEM/BS). (c) Flank wear pattern after β-Si_3N_4–tool steel machining (SEM/BS).

4. Discussion

4.1. Thermal and mechanical loading in high speed cutting

In semi-orthogonal cutting there are three force components acting in the X–Y–Z directions of space (Fig. 14) [4]. Two shear zones — the so-called primary shear zone (1) and secondary (2), or "flow", shear zone [4, 17]—are initiated from the chip development point. The two shear zones are highly localized energy sources. The primary shear zone extends from the new surface generation point O to the point where the material separates from the workpiece surface O'. It is related to the shear angle ϕ which is given by [3]

$$\tan \phi = \{(t_1/t_2) \cos \alpha\}/\{1-(t_1/t_2) \sin \alpha\} \tag{4}$$

where t_1 is the chip thickness before the primary shear plane, t_2 is the chip thickness after the primary shear plane and α is the rake angle.

The plastic strain τ in the primary shear plane is a function of the angles ϕ and α [4]

$$\tau = \cos \alpha/\{\sin \phi \cos(\phi - \alpha)\} \tag{5}$$

In high speed cutting, the strain rates in the primary shear region can attain values up to 10^5 s^{-1} [3], but the strain is usually below $\tau = 5$.

The secondary shear or "flow" zone may be observed when high normal forces bring the real contact area close to the apparent contact area of the surfaces. The

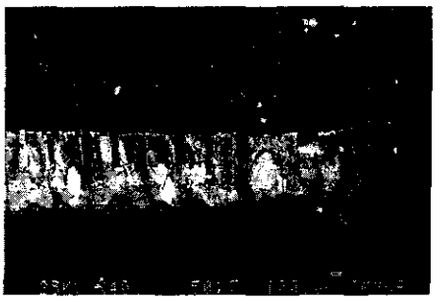

(a)

(b)

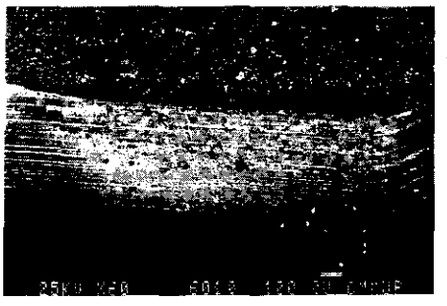

(c)

Fig. 10. (a) View of the rake and clearance faces after tool steel machining (β-Si_3N_4; 3.6 m s^{-1}; $t = 15$ s) (SEM/BS). (b) Chemically contrasted wear pattern after CeSiAlON–tool steel machining (3.9 m s^{-1}; $t = 12$ s) (SEM/BS). (c) Wear patterns of the CeSiAlON insert after gray cast iron machining with high material removal ($M_r = 1170 \times 10^{-6}$ m^3) (SEM/BS).

tangential load required to move the chip over the rake face is no longer proportional to the normal load as in the conventional tribological pairs, but it becomes dependent on the shear strength of the chip material. Relative movement due to shear in the chip material some tens of micrometers above the sticking contact counteracts the tool seizure at the chip–tool contact interface. The seizure in the flow zone has been experimentally verified by rapid-stop tests during cutting [4, 17]. Shear strain values as high as 640 have been calculated in the flow zone [4]. This strain is two orders of magnitude greater than the strain values in the primary shear plane.

Due to the brittleness of ceramic materials, tool geometries with a negative rake angle are used which result in a low shear angle ϕ and a large rake contact area; thus the conditions for seizure are enhanced when ceramic tools are used.

The heat generated during cutting has two components: the heat generated on the primary shear plane Q_s and the heat generated on the flow zone Q_F. Q_s represents a small contribution to the tool heating Q_F is directly proportional to the cutting speed [4]

$$Q_F = (F_F V \tan \phi)/J \tag{6}$$

where F_F is the feed force, V is the cutting speed and J is the mechanical heat equivalent.

The thermal load on the tool is mostly due to the heat generation by the deformation work of the chip, mainly in the flow zone. Temperatures up to 1200 °C are easily

(a)

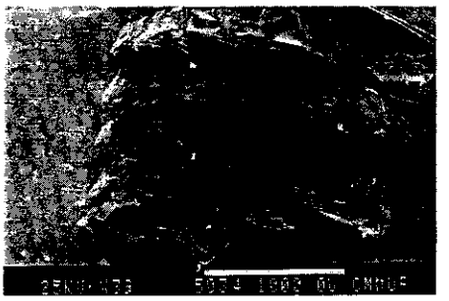

(b)

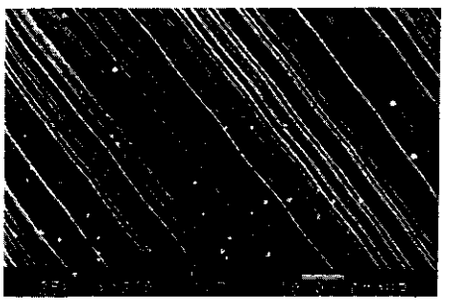

(c)

Fig. 11. (a) Low magnification of the tool steel chip (SEM). (b) Discontinuous-type chip from β-Si_3N_4–gray cast iron machining (SEM). (c) High magnification (SEM) of the surface of the tool steel chip in contact with the ceramic.

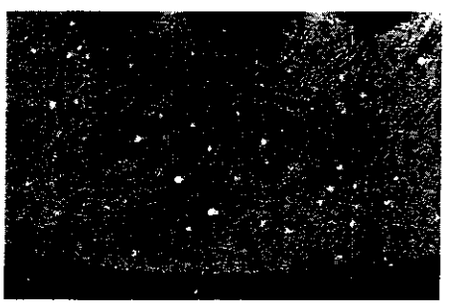

Fig. 12. Longitudinal section of the tool steel chip with carbide contrasting (optical micrograph; original magnification ×250).

attained in high speed cutting with ceramic inserts [5] and so the material is subjected to extreme mechanical and chemical loading.

Mechanical loading is related to workpiece primary shear plane strength σ_S or to the mean shear strength at the rake face σ_R through the loads required to deform the chip in those planes [4]

$$\sigma_S A_S = F_C \cos \phi - F_F \sin \phi \tag{7}$$

where A_s is the primary shear plane area, F_C is the cutting force and [4]

TABLE 5

Cutting parameters and wear results in turning tests

Tool–workpiece	Cutting time (s)	DOC (10^{-3} m)	Feed (10^{-3} m)	Cutting speed (m s^{-1})	Removal rate (10^{-6} m^3 s^{-1})	VB (10^{-3} m)	KM (10^{-3} m)	KT (10^{-3} m
A–GI	610	2	0.25	3.1	1.6	0.108	0.275	0.190
A–GI	265	2	0.25	8.0	4.0	0.132	0	0
A–GI	231	2	0.25	11.2	5.6	0.176	0	0
A–TS	35	1	0.25	3.6	0.9	[a]	0.628	[a]
A–TS	15	1	0.25	3.6	0.9	0.776	0.512	0.300
A–TS	15	1	0.25	3.6	0.9	0.848	0.504	0.285
B–GI	15	1	0.25	3.6	0.9	0	0	0
B–GI	67	2	0.25	3.6	1.8	0.040	0	0
B–TS	15	1	0.25	3.6	0.9	0.836	0.512	0.250
B–TS	15	2	0.25	3.6	1.8	0.824	0.544	0.240
B–TS	15	4	0.25	3.6	3.6	0.832	0.516	0.275
B–TS	52	1	0.25	2.6	0.7	[a]	0.803	0.275
C–GI	275	2	0.25	8.5	4.3	0.146	0	0
C–GI	125	2	0.25	12.2	6.1	0.136	0	0
C–GI	85	4	0.25	11.0	11.0	0.220	0	0
C–TS	12	2	0.25	3.9	2.0	0.520	0.224	0.110
C–TS	12	4	0.25	3.9	3.9	0.532	0.320	0.100
C–TS	60	1	0.25	2.4	0.6	0.980	0.448	0.225

A, B, β-Si_3N_4 inserts; C, CeSiAlON insert; GI, gray iron; TS, tool steel.
[a]Edge collapse.

$$\sigma_R A_R = F_F \tag{8}$$

where A_R is the rake contact area.

The chip width w is almost equal to the depth of cut. The rake contact can be adequately described by the length of contact L. This variable is also related to the workpiece material through the chip deformability. In extreme cases, the deformability can result in discontinuous fragments due to the brittle response in the primary shear plane or in a large contact area for the ductile chips of pure metals. Lubricants can decrease the effective length of contact.

The value of the shear angle ϕ can be calculated from the minimum energy theory [4]. From the following expression of the total work rate dW/dt, it can be graphically established that the shear angle ϕ decreases with increments of L, σ_S and V [4]

$$dW/dt = dW_R/dt + dW_S/dt = V\sigma_S\{(wL)\tan\phi + (t_1 w/(\sin\phi\cos\phi)\} \tag{9}$$

where W_S is the primary shear plane work, W_R is the secondary shear plane work and w is the chip width (depth of cut).

The contact area (wL), workpiece strength σ_S and speed all increase the cutting forces and the total work (eqns. (7) and (9)).

The movement of the workpiece as a fresh surface over the tool clearance face must also be considered. The normal pressure acting on this face is much lower than

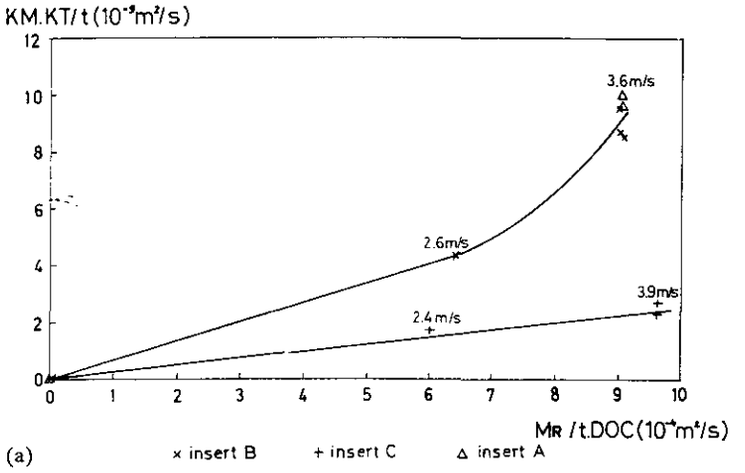

(a) × insert B + insert C △ insert A

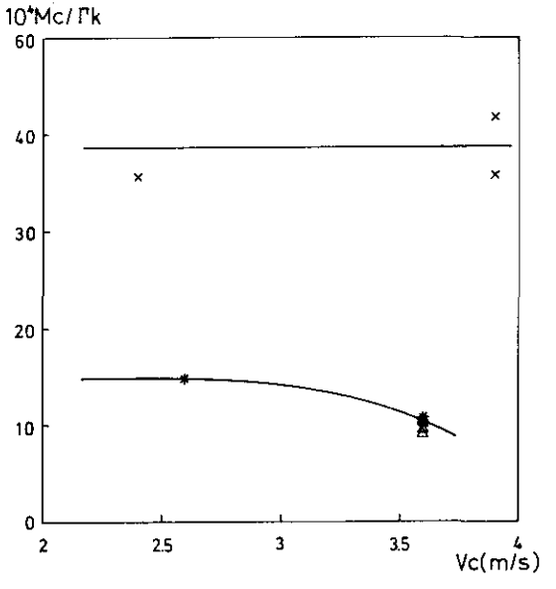

(b) ✱ insert B × insert C △ insert A

Fig. 13. (a) Dependence of crater wear rate on removal rate normalized to the depth of cut for tool steel machining. (b) Dependence of crater wear resistance on cutting speed in tool steel machining.

the normal pressure on the rake face. Yet, a worn surface soon develops as flank wear by rubbing. Heat is generated by sticking and friction at this contact. The corresponding heat term adds to the heat from the workpiece and the thermal diffused heat which comes through the tool to this contact surface. The high temperature and the mechanisms already described for the crater contact can be repeated. However, microcutting by fragments of the rake contact or by hard constituents of the workpiece material has been observed to be the dominant mode of flank wear [17].

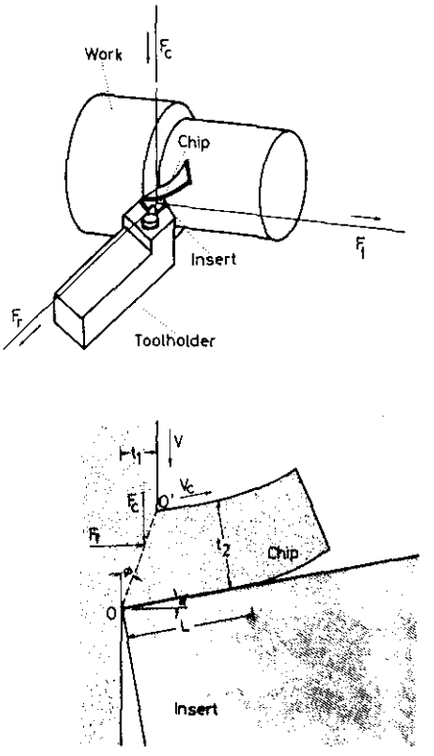

Fig. 14. Forces which act on the ceramic cutting tools and geometric features of the chip: F_c, cutting force; F_F, feed force; F_R, radial force; t_1, feed; t_2, chip thickness; V, cutting speed; V_C, chip speed; L, contact length; ϕ, primary shear angle; α, rake angle.

The overall mechanically and thermally induced stresses and temperature distribution during metal cutting with ceramic tools have been treated by finite-element analysis [18]. Consistent knowledge of the tool and workpiece properties and the tool–workpiece interaction is included in the models in order to rank the tool performances. In addition to these general considerations on mechanical and thermal modelling in cutting, thermal shock itself [18, 19] plays an important role in the failure of the ceramic inserts. The higher thermal conductivity and lower thermal expansion of Si_3N_4-based materials as compared with other ceramics, namely the "white" ceramics, renders the contribution of thermal shock negligible in this particular system.

4.2. Wear behavior of Si_3N_4-based tools

A comparison of the wear lands in Fig. 5(a) and 5(b) confirms the markedly distinct wear behavior of the Si_3N_4-based tools in the cutting of steel and gray cast iron [1, 5, 20].

High values of the forces acting on the tool were generated in the machining of TS2080 steel as a result of the material work strength (eqns. (7) and (8)) and the continuous chip type. Intense shearing occurred in the primary shear zone and flow zone during chip formation due to the seizure on the rake face. The shape of the

carbide alignments revealed a large gradient of the shear strain rates, zero speed being approached at the tool–chip interface (Fig. 12), thus corroborating the seizure mechanism. As the hot strength of CeSiAlON is high, the metallic seized film was retained on the crater surface (Fig. 7(c) and 7(d)).

Following eqns. (5), (6) and (9), sticking and the large real contact area, together with the high cutting speed and the resulting high cutting forces, locally promote heat generation. The high temperature and the intimate chip–tool contact under seizure conditions activate chemical wear in these types of ceramics.

Chemical wear can operate through dissolution of the tool material in the chip [9] or by corrosion of the ceramic intergranular phase by the metallic elements [21, 22]. High chemical dissolution wear rates of Si_3N_4 in metastable ferrite have been predicted from thermodynamic calculations [9]. The interaction parameters of elemental solid solutions must be accounted for in the calculation of the silicon and nitrogen activities if the chemical dissolution of the tool is to be determined during the cutting of different iron alloys. The widths of the reaction zones observed in interdiffusion studies of steel–Si_3N_4 contacts [5] are much larger than the corresponding zones of the gray cast iron–Si_3N_4 contacts. Both alloys have ferrite as the iron-rich phase. Chromium as an alloying element in steel is known to increase the extent of the interdiffusion zone of the steel–Si_3N_4 contact [23]. The TS2080 steel has a high chromium content and this may increase the Si_3N_4 tool dissolution wear in the present study. The interdiffusion tests may reflect the chemical potential for tool–workpiece reaction in cutting. CeO_2 additives are promising sintering aids for Si_3N_4 (when compared with Y_2O_3) [5] as the interdiffusion zone is smaller in the CeO_2-doped Si_3N_4 samples and the corresponding tool wear during steel cutting is also lower. The elements of the ceramic composition could not be detected by EDS chemical analysis on the underside of the chip as the ratio of the tool wear land volume to the chip volume was very low.

The SEM–EDS results indicate that the chemical wear proceeded through local corrosion of the intergranular phase by the metallic elements. Calcium and aluminum impurities of the ceramic tool were selectively concentrated together with cerium at the crater trailing edge (Fig. 9(b)). There was a discontinuity between this deposit and the extended glassy deposit beyond the crater (Fig. 7(a)). From the seizure mechanism discussed above [4, 24], there should be no access of atmospheric oxygen to the crater. The deposit must be different from the glassy layer observed in the intermittent chip contact zone. In the extended glassy zone, iron and chromium were detected by SEM–EDS, but not the ceramic grain boundary element cerium or the impurities calcium and aluminum. Calcium is an impurity from the amorphous intergranular phase of the Si_3N_4 ceramic and cerium is the main additive of the sintering-aiding liquid. Cerium does not go into solid solution in the Si_3N_4 crystalline lattice. The concentration of iron in the dragged material was above the average detected level in the crater itself. As the ceramic grain boundary phase is rich in oxygen, oxygen from the ambient atmosphere is not required for the chemical reaction between iron and ceramic in the crater [6]. Preferential corrosion of the intergranular phase [21, 22] by reaction between the intergranular SiO_2-rich amorphous phase and the iron with the formation of an iron silicate glass (a fayalite-like reaction product [25]) decreased the grain boundary strength. Calcium and aluminum as grain boundary impurities further decreased the viscosity of the reaction product. Chemical wear by preferential corrosion of the intergranular phase was also observed to be the wear mechanism of the Si_3N_4–steel sliding contacts in the pin-on-disk tests; the iron and cerium correlation reported in Fig. 3(b) is the result of the reaction kinetics between the iron and the cerium-rich grain boundary phase.

As silicon nitride matrix disruption occurs by intergranular flowing, Si_3N_4 grains pull out [26] and plough the ceramic surface. This could be seen throughout the crater land (Fig. 7(b)) where iron- and chromium-rich deposits at the entrance were followed by grain pullout and increasingly intensive abrasive wear towards the crater end (Figs. 9(b) and 11(c)).

The main characteristic of the CeSiAlON–steel contact was the improved mechanical resistance to the effects of seizure and corrosion. The crater was extensively coated by iron and chromium adhesions (Fig. 7(c)). Abrasion from grain ploughing was restricted to the crater end. The worn land itself was also less mechanically damaged (Fig. 7(d)) than the entrance zone of the β-Si_3N_4 contacts (Fig. 7(b)). The chemical reaction between the chip material and the intergranular layer resulted in impurity segregation, namely calcium enrichment of the seized layer. Yielding and accumulation of intergranular-originated deposits at the crater end were not observed in this system. The higher hot strength of the ceramic underneath the reaction layer preserved the layer adherence. The observation that nitrogen-rich glasses of SiAlON compositions are creep resistant [15, 16, 27] agrees with the present results. The data in Table 2 for both Si_3N_4 materials show similar fracture toughness (and aspect ratio) but improved room temperature hardness of the CeSiAlON material. The higher room temperature hardness values of the fine grain CeSiAlON material in comparison with β-Si_3N_4 (Table 2) are expected to be retained at high temperatures [27]. Since the abrasive wear resistance is increased by the material hardness [28], better performance will also result from the higher value of the hot hardness of the CeSiAlON insert.

The speed corresponding to the inflexion point of the wear rate *vs.* removal rate (Fig. 13(a) and 13(b)) can be used as a new definition of the cutting speed limit of the Si_3N_4 inserts. This point is related to the onset of enhanced grain boundary corrosion, softening of the intergranular phase, grain pullout and intensive ploughing of the crater surface of the Si_3N_4 inserts, as described above.

The mechanical loads and temperatures calculated for the contact surface of the clearance face are lower than the corresponding values for the rake contact surface [4, 18]. A large, smeared layer of material from the workpiece adherent to the worn surfaces was a widespread feature of flank wear in the ceramic–steel contacts (Fig. 10(a) and 10(b)). Break up of the small workpiece–tool adhesive joints in the clearance worn land indicated adhesive wear (Fig. 9(c)). Flank wear is primarily oxidative in nature [17]. Rubbing in the trailing edge of the worn land of the CeSiAlON insert suggested a thinner and less abundant adhesion layer. This composition combined high abrasion resistance with a lower oxidation rate, resulting in lower flank wear when compared with β-Si_3N_4 (Table 5).

The edge retention in the severe conditions of the present tests can be explained by the good performance of the Si_3N_4-based materials in terms of strength, namely fracture toughness and thermal shock resistance [5, 19] (Fig. 6). Notch wear by local tensile stress concentration [18] and/or stress gradients [5, 19] at the transition point between the tool and the workpiece was not observed. This can again be explained by the low sensitivity to thermal loads and the high resistance to thermal-shock-induced fracture of the Si_3N_4 inserts in relation to other ceramic inserts.

The characteristic features of the worn rake face after the cutting of gray cast iron are shown in Fig. 6(c) for the β-Si_3N_4 tool and in Fig. 6(d) for CeSiAlON. The manganese-rich dragged film in the crater end zone was followed by iron oxide deposition in the intermittent contact region. The manganese-rich deposits of both tool materials had a similar morphology. However, since sulfur could not be detected by EDS analysis for the CeSiAlON test at high removal rate, the high temperature

of the contact might have induced sulfur oxidation. MnS lubricates [20] the chip–rake face contact. The workpiece strength and plasticity of gray cast iron are lower than for steels. The brittle chip (Fig. 11(b)), together with MnS lubrication, can drastically reduce the real contact area, thus decreasing the work of cutting (eqn. (9)) and the heat (eqn. (6)). Lubricated sliding instead of seizure then becomes the main mechanism of chip–rake surface interaction. Under lubricated conditions, any contribution from chemical wear is of secondary importance to the effects of microhardness [22] and an improvement in crater wear resistance (Table 5), in comparison with that observed in steel cutting, was obtained. For high removal rates (11×10^{-6} m^3 min^{-1}) some wear occurred under the extreme conditions of the test and fine grooving of the rake surface was observed (Fig. 7(f)). As the fundamental wear mechanism was abrasion, an excellent rank position of the Si_3N_4-based tools in the machining of chemically non-reactive alloys was predicted by Evan's hardness–toughness criterion [1, 28].

Flank wear was observed at the leading edge of the clearance face, with the worn surface showing the same features as the rake face. The contact surface beyond the leading edge of the clearance face was preserved by a covering of metal (Fig. 10(c)); ceramic surface machining grooves were clearly observed after testing with high metal removal. The adherence of slag [22] on this surface was different from the thin tribological layer observed on the rake face as, in the latter, the discontinuous chip and high temperature MnS lubrication rendered the crater surface almost clean.

From the microstructural description and the cutting model presented in this work, the main difference in the behavior of the two iron alloys can be attributed to the distinct interactions with the tool of a high strength, high temperature deformable alloy (tool steel) and a brittle composite-like alloy with additional self-lubricating effects at high temperatures (gray cast iron).

4.3. Comparison between wear tests and cutting tests

The tribological coefficients (μ and K) for gray cast iron–ceramic and tool steel–ceramic pairs were similar [29] (Table 4). The corresponding worn ceramic surfaces were generally polished or smoothly abraded (Fig. 1). The pin-on-disk test coefficients can be compared with similar results in the literature [29, 30]. The different wear rates of the ceramic inserts during the cutting of the two iron alloys were not observed in the pin-on-disk test in air at the load and speed conditions investigated. Polished surfaces can be produced mechanically or chemically. It is difficult to determine the main mechanism of polishing when a non-adherent debris layer is present, as seems to occur in these contacts [29]. Mechanical damage was not extensive, with a small contribution of abrasion to the wear (Figs. 1(b) and 2(a)). Wear was probably the result of sliding, which produced surface oxidation of both materials of the wear couple. Silicate glass development is thermodynamically favorable in air. Silicate glassy layers were observed on the pin surface (Fig. 2(b)) and on the wear tracks of the metallic disks. The wear debris was rich in Si–Fe composite glassy plates (Fig. 4). These tribochemical products did not protect the ceramic surface due to lack of adhesion. This can be related to the high friction coefficient values, which sometimes reached 0.85 (Table 4). The glassy products originated from the SiO_2 and CeO_2-rich ceramic intergranular phase by reaction with iron and oxygen, as corroborated by the correlation between the cerium concentration, an intergranular element indicator, and the iron concentration on the worn ceramic surface (Fig. 3(b)).

Several sources of discrepancy between the results of cutting tests and pin-on-disk tests have been reported [7, 25]. Unless a solid lubricant such as MnS is preserved at the contact, the reaction of iron with oxygen increases the chemical wear of the

ceramic in both types of tests, the reaction rate being enhanced at the grain boundary phase. The nitrogen-rich SiAlON exhibits a better resistance to the softening of the grain boundary phase resulting from this reaction, and thus the concurrent abrasion is reduced. The following features differentiate the two tests for the iron alloy–Si_3N_4 pairs investigated in this study.

(i) High stress, high temperature continuous loading of the ceramic surface and seizure can be created during machining depending on the chip deformation work.

(ii) An interfacial oxidized layer is developed on the repetitive, low stress conventional pin-on-disk contacts in air. The thickness of the composite silicate-like layer built up from debris accumulation decreases the chemical gradients in opposition to the fresh workpiece–tool contact during cutting and dictates the tribology of the contacting surfaces. By matching the loads, surface speed, temperature and oxygen activity of the contacting surfaces, the effects of chemical wear, softening of the intergranular phase, grain pullout and ploughing can be approximated in the pin-on-disk and cutting tests. This would be feasible in conventional testing machines with convenient pin geometry, after upgrading the control of the environmental atmosphere and temperature.

5. Conclusions

The nature of the markedly distinct wear behavior of the Si_3N_4-based cutting tool during the machining of gray iron and tool steel was studied by SEM–EDS observation of the worn contacts, investigation of the chip geometry and modelling of the metal cutting process. The wear mechanisms were also investigated by conventional pin-on-disk tests in air, but build-up of a debris layer and reaction with atmospheric oxygen masked most of the differences between the materials. Machining of the iron alloys with the Si_3N_4 inserts produced the following major features.

(i) In the machining of high strength tool steel, a high stress, high temperature environment is created and the seizure condition becomes increasingly important with increasing cutting speed, resulting in chemical corrosive paths through the stacked layer between the workpiece and the ceramic tool. Disruption of the ceramic matrix promotes severe high temperature abrasion on the tool rake surface that can be counteracted by a nitrogen-rich intergranular phase. The refractoriness and microhardness of the ceramic are important parameters in tool evaluation.

(ii) The brittle behavior of the gray cast iron chip and MnS lubrication result in a system of low cutting forces and low temperatures at the contact surface. Extensive chemical reactions are thus avoided.

Acknowledgment

The financial support from JNICT and Minas e Metalurgia under the research contract 87/80 MATR is gratefully acknowledged.

References

1 J. G. Baldoni and S. T. Buljan, *Ceram. Bull.*, *67* (2) (1988) 381–387.
2 E. D. Whitney, *Powder Metall. Int.*, *15* (4) (1983) 201–205.

3 G. E. Dieter, *Mechanical Metallurgy*, McGraw-Hill, New York, 1976.
4 E. M. Trent, *Metal Cutting*, Butterworths, Guildford, 1984.
5 S. T. Buljan and S. F. Wayne, *Wear, 133* (1989) 309–321.
6 M. Olsson, S. Soderberg, S. Jacobson and S. Hogmatk, *Int. J. Mech. Tools Manufact., 29* (3) (1989) 377–390.
7 M. Olsson, B. Stridh, S. Soderberg and U. Jansson, *Wear, 124* (1988) 195–216.
8 S. T. Buljan and S. F. Wayne, *Adv. Ceram. Mater., 2* (4) (1987) 813–816.
9 B. M. Kramer and N. P. Suh, *ASME Trans. J. Eng. Ind., 102* (3) (1980) 303–309.
10 E. Tani, S. Umebayashi, K. Kishi, K. Kobayashi and N. Nishijima, *Am. Ceram. Soc. Bull., 65* (9) (1986) 1311–1315.
11 K. Niihara and T. Hirai, *Powder Metall. Int., 16* (5) (1984) 223–226.
12 E. F. Underwood, *Quantitative Stereology*, Addison-Wesley, New York, 1970.
13 G. Wotting, B. Kanka and G. Ziegler, in S. Hampshire (ed.), *Non-Oxide Technological and Engineering Ceramics*, Elsevier Applied Science, London, 1986, pp. 83–95.
14 L. J. Gauckler and G. Petzow, in F. Riley (ed.), *Nitrogen Ceramics*, Noordhoff, Leyden, 1977, 41–60.
15 D. R. Messier and A. Broz, *Commun. Am. Ceram. Soc., 65* (1982) C-123.
16 S. Hampshire, P. A. Drew and K. H. Jack, *Commun. Am. Ceram. Soc., 67* (1984) C-46–C-47.
17 J. A. Schey, *Tribology and Metalworking*, American Society for Metals, Metals Park, OH, 1983.
18 H. K. Tonshoff and S. Bartsch, *Ceram. Bull., 67* (5) (1988) 1020–1025.
19 S. F. Wayne and S. T. Buljan, *Ceram. Eng. Sci. Proc., 9* (9–10) (1988) 1395–1408.
20 A. N. Grearson, L. Hielert, N. Ingelstrom and H. Pastor, *Ind. Ceram., 775* (9) (1983) 615–621.
21 E. O. Ezugwu and J. Wallbank, *Mater. Sci. Technol., 3* (1987) 881–887.
22 G. N. Babini, A. Bellosi, R. Chiara and M. Bruno, *Br. Ceram. Proc., 37* (1986) 109–116.
23 M. J. Bennett and M. R. Houlton, *J. Mater. Sci., 14* (1979) 184–196.
24 Z. Zehua, *Wear, 121* (1988) 173–182.
25 D. Agranov, D. Brandon and R. Wertheim, *Ind. Ceram., 8* (4) (1988) 192–197.
26 M. K. Brun and M. Lee, *Ceram. Eng. Sci. Proc., 4* (7–8) (1983) 646–662.
27 T. Ekstrom, *Mater. Sci. Eng., A109* (1989) 341–349.
28 A. G. Evans and T. R. Wilshaw, *Acta Metall., 24* (1976) 939–956.
29 M. G. Gee, *Br. Ceram. Proc., 39* (1987) 141–153.
30 G. W. Stachowiak, G. B. Stachowiak and A. W. Batchelor, *Wear, 132* (1989) 361–381.